Aerospace Science and Technology 143 (2023) 108717

Contents lists available at ScienceDirect

Aerospace Science and Technology

journal homepage: www.elsevier.com/locate/aescte

Detonation wave structure and thrust variation of a ram accelerator with different projectile velocities

Jiahao Shang [a,b], Kuanliang Wang [c,*], Aifeng Wang [d], Qiu Wang [a,*], Wei Zhao [a,b]

[a] State Key Laboratory of High Temperature Gas Dynamics, Institute of Mechanics, Chinese Academy of Sciences, Beijing 100190, China
[b] School of Engineering Science, University of Chinese Academy of Sciences, Beijing 100049, China
[c] School of Aerospace Engineering, Beijing Institute of Technology, Beijing 100081, China
[d] Aero Engine Academy of China, Aero Engine Corporation of China, Beijing 101304, China

ARTICLE INFO

Keywords:
Ram accelerator
Detonation
Oblique detonation wave
Recirculation zone

ABSTRACT

A study was conducted to investigate the effect of velocity on the detonation wave structure and thrust of a ram accelerator using a simulation of a premixed, reacting flow over a conical projectile. The simulation involved solving the compressible reactive Navier-Stokes equations with a detailed chemical model in a channel with a supersonic stoichiometric hydrogen-oxygen inflow. Results showed that at projectile velocities lower than the Chapman-Jouguet detonation velocity, a thermally choked unstart occurs. As the projectile velocity increases, the overdriven detonation mode, trans-detonative mode, and super-detonative mode successively form. The maximum thrust was achieved at the lower velocity limit under the overdriven normal detonation condition, but decreased continuously as an oblique detonation wave formed. The super-detonative mode was distinguished by the smoothness of the tail thrust derived from the recirculation zone and ignition before the conical ramp led to an unstart at the upper velocity limit.

Introduction

The ram accelerator is a hypervelocity mass-driver system, which accelerates a finned projectile supersonically and hypersonically through a tube pre-filled with a combustible gas mixture [1–3]. The combustible mixture is compressed by the projectile nose, and then a series of detonation waves is induced that generates the thrust with the high-pressure burned gas. As a ramjet-in-tube concept, hypersonic propulsion of a ram accelerator is based on detonation combustion mainly with an oblique detonation wave (ODW).

An ODW is a detonation wave that stabilizes on an obstacle in supersonic flows of detonable mixtures, and the reaction is initiated by an oblique shock wave (OSW). Various studies have focused on the OSW–ODW transition [4,5], the ODW surface instability [6,7], and the wave structure of the initiation region [8]. When the projectile velocity, configuration, and mixture composition are varied, different ODW structures can exert different, high pressures on the projectile. This has prompted experimental [9–11] and computational [12–14] studies to understand the structure and stability of ODWs near a projectile. An extensive series of studies was conducted by Hertzberg et al. [1,10], who found five modes of ram accelerator operation over a range of projectile velocities including two subsonic combustion modes (one of which involves thermally choked combustion), a normal overdriven detonation mode, and two oblique detonation modes (the trans-detonative and super-detonative modes). In the super-detonative mode, Choi et al. [13] carried out a variety of numerical studies on how ram accelerator operation depends on ignition source, viscous effects, and fluid dynamic parameters (physical size, inflow pressure, and temperature). Moreover, Bachman et al. [15] investigated the augmentation of the leading oblique shock wave by the burning boundary layer during ODW formation.

Analyses have shown that the detonation structure experienced by the projectile changes significantly but remains stable during continuous acceleration. However, the computational results obtained were limited because these simulations did not cover the overall projectile velocity range. Therefore, this study explores the detonation structure over the entire operating velocity range. First, the main flow of the super-detonative mode is analyzed, and then the lower and upper limits of operating velocity are determined. At the lower limit, the wave structure is found to be an overdriven normal detonation, and at even lower velocities, a thermal choking unstart occurs. The upper limit occurs in the super-detonative mode, and the upper unstart is caused by augmentation of the leading OSW. The thrust is analyzed from the sub-detonative

* Corresponding author.
E-mail addresses: wangkuanliang@bit.edu.cn (K. Wang), wangqiu@imech.ac.cn (Q. Wang).

https://doi.org/10.1016/j.ast.2023.108717
Received 29 May 2022; Received in revised form 7 April 2023; Accepted 1 November 2023
Available online 4 November 2023
1270-9638/

limit to the super-detonative limit, and the trans-detonative and super-detonative modes are compared.

Physical models and numerical methods

This study developed a density-based OpenFOAM solver that combines rhoCentralFoam and rhoReactingFoam for high-speed reactive flows. The compressible Navier–Stokes equations were combined with a chemical reaction mechanism and solved. The conservation equations of mass, momentum, energy, and species are expressed as

$$\frac{\partial \rho}{\partial t} + \nabla\cdot(\rho u) = 0, \tag{1}$$

$$\frac{\partial \rho u}{\partial t} + \nabla\cdot(\rho u u) = -\nabla p + \nabla\cdot\tau, \tag{2}$$

$$\frac{\partial \rho h}{\partial t} + \nabla\cdot(\rho h u) = \frac{\partial p}{\partial t} - \nabla q + \nabla\cdot(\tau\cdot u) + \dot{q}, \tag{3}$$

$$\frac{\partial \rho Y_\mathrm{i}}{\partial t} + \nabla\cdot(\rho Y_\mathrm{i} u) + \nabla\cdot J_\mathrm{i} = \dot{\omega}_\mathrm{i}, \tag{4}$$

where

$$\dot{q} = \sum_{\mathrm{i}=1}^{\mathrm{n}} \dot{\omega}_\mathrm{i} \Delta h^0_{\mathrm{f,i}} \tag{5}$$

where ρ denotes the reactive mixture density, $\boldsymbol{u}$ is the velocity, t is the time, h is the specific total enthalpy of the mixture, $\dot{q}$ is the energy equation source, $\dot{\omega}_\mathrm{i}$ is the production/consumption rate of the species i, and Y_i is the mass fraction of species i ($i = 1, 2, \ldots, \mathrm{n}$). The pressure p can be calculated from the state equation for an ideal gas, $p = \rho R T = \rho T R_\mathrm{u} \sum_{i=1}^{\mathrm{n}} Y_\mathrm{i} W_\mathrm{i}^{-1}$, with R_u the universal gas constant and W_i the molecular mass of species i. The total enthalpy h is calculated from

$$h = \sum_{\mathrm{i}=1}^{\mathrm{n}} h_\mathrm{i} Y_\mathrm{i}, \tag{6}$$

and the species total enthalpy is written as

$$h_\mathrm{i} = \Delta h^0_{\mathrm{f,i}} + h_{\mathrm{s,i}}, \tag{7}$$

$$h_{\mathrm{s,i}} = \int_{T_0}^{T} C_{\mathrm{p,i}} dT, \tag{8}$$

$$C_{\mathrm{p,i}} = R((((a_4 T + a_3)T + a_2)T + a_1)T + a_0), \tag{9}$$

where $\Delta h^0_{f,i}$ and $h_{s,i}$ are the species formation enthalpy and sensible enthalpy, and $C_{p,i}$ is the specific heat of species i at constant pressure.

The stress tensor $\boldsymbol{\tau}$ is calculated from

$$\tau = \mu\left[\nabla u + (\nabla u)^{\mathrm{T}}\right] + \lambda(\nabla\cdot u)I, \tag{10}$$

where μ is the dynamic viscosity according to the Sutherland model, and λ is the second viscosity, expressed as

$$\mu = \frac{A_\mathrm{s}\sqrt{T}}{1 + T_\mathrm{s}/T}, \tag{11}$$

$$\lambda = -\frac{2}{3}\mu. \tag{12}$$

The Sutherland coefficients are $A_\mathrm{s} = 1.458\times10^{-6}$ and $T_\mathrm{s} = 111$ K.

The heat flux $\boldsymbol{q}$ in the energy equation is written as

$$q = -k\nabla T, \tag{13}$$

where k is the thermal conductivity and is computed from the specific heat at constant volume C_v via

$$k = \frac{(9\gamma - 5)}{4}\mu C_\mathrm{v}. \tag{14}$$

In Eq. (4), the reaction rate constants for elementary reactions are calculated using the Arrhenius law. J_i is the mass diffusive flux expressed as

$$J_\mathrm{i} = \rho D_\mathrm{i} \nabla Y_\mathrm{i}, \tag{15}$$

where D_i is the diffusion coefficient calculated from the diffusion model

$$\rho D_\mathrm{i} = \frac{\mu}{S_{\mathrm{ti}}}, \tag{16}$$

where S_{ti} is the Schmidt number, which is set as constant for all species.

Fig. 1 shows the computational domain used in this work. The axisymmetric tube domain was of length 200 mm with an outside diameter of 50 mm. The projectile diameter was 25 mm and the wedge angle was 11.8° The upper and lower boundaries were adiabatic, no-slip walls. And a zero a zero-gradient condition was applied in the outflow boundary. The premixed gas was a stoichiometric H_2/O_2 mixture with a frozen reaction to induce an inert shock wave and initiate a detonation in the first 100 μs. The inflow mixture was maintained at $P_0 = 101.35$ kPa and $T_0 = 300$ K, under which conditions the Chapman–Jouguet (C–J) detonation velocity is about 2843 m/s. The non-dimensional projectile velocity $V_\mathrm{p}/V_\mathrm{CJ}$ was varied from 0.8 to 2.4 to cover the entire start range. The simulations used the chemical reaction mechanism proposed by Ó Conaire [16] with 11 components (H, O, OH, H_2, O_2, H_2O, HO_2, H_2O_2, N_2, Ar, and H_2) and 19 reactions (Table 1), which has been verified and widely used for combustion calculations. The computational structure grid size was fixed at $dx = 100$ μm, and a resolution study was performed to test the sensitivity of the system, as presented in the Appendix.

Results and discussion

This paper focuses on the gas dynamics and combustion characteristics of ram accelerators with varying projectile velocities. The initial condition was assumed to be an initial Mach number of 7.9 with a corresponding non-dimensional projectile velocity of 1.5. Fig. 2 shows the steady-state contours of the temperature and pressure, which provide a typical OSW–ODW transition structure in front of the projectile nose. The triple wave point occurs after the expansion platform and settles on the conical ramp connecting two detonation sections. There is a regular reflection of the upper detonation wave on top of the upper wall. The lower section of the detonation wave stretches to the projectile like a normal detonation wave. An expanding wave downstream of the conical ramp interacts with the reflected oblique wave, and a recirculation zone forms at the tail owing to the confined geometry and shock–shock interaction. Consequently, the high-temperature and high-pressure burned gas expands through the conical nozzle and generates a high thrust force.

As Fig. 3 illustrates, the global wave system remains relatively stable

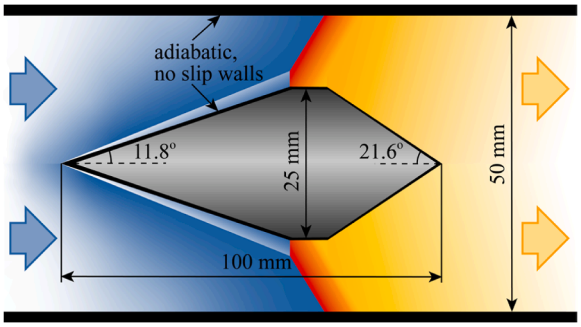

Fig. 1. Schematic of the computational domain.

Table 1
H_2/O_2 reaction model [16].

Reactions		A	n	E_a
(1)	$H + O_2 = O + OH$	1.91E+14	0.00	1.644E+04
(2)	$O + H_2 = H + OH$	5.08E+04	2.67	6.292E+03
(3)	$H_2 + OH = H_2O + H$	2.16E+08	1.51	3.430E+03
(4)	$O + H_2O = OH + OH$	2.97E+06	2.02	1.340E+04
(5)	$H_2 + M = H + H + M$	4.57E+19	−1.40	1.051E+05
(6)	$O + O + M = O_2 + M$	6.17E+15	−0.50	0.000E+00
(7)	$O + H + M = OH + M$	4.72E+18	−1.00	0.000E+00
(8)	$H + OH + M = H_2O + M$	4.50E+22	−2.00	0.000E+00
(9)	$H + O_2 + M = HO_2 + M$	3.48E+16	−0.41	−1.120E+03
	$H + O_2 = HO_2$	1.48E+12	0.60	0.000E+00
(10)	$HO_2 + H = H_2 + O_2$	1.66E+13	0.00	8.200E+02
(11)	$HO_2 + H = OH + OH$	7.08E+13	0.00	3.000E+02
(12)	$HO_2 + O = O_2 + OH$	3.25E+13	0.00	0.000E+00
(13)	$HO_2 + OH = H_2O + O_2$	2.89E+13	0.00	−5.000E+02
(14)	$HO_2 + HO_2 = H_2O_2 + O_2$	4.20E+14	0.00	1.198E+04
	$HO_2 + HO_2 = H_2O_2 + O_2$	1.30E+11	0.00	−1.629E+03
(15)	$H_2O_2 + M = OH + OH + M$	1.27E+17	0.00	4.550E+04
	$H_2O_2 = OH + OH$	2.95E+14	0.00	4.840E+04
(16)	$H_2O_2 + H = H_2O + OH$	2.41E+13	0.00	3.970E+03
(17)	$H_2O_2 + H = HO_2 + H_2$	6.03E+13	0.00	7.950E+03
(18)	$H_2O_2 + O = OH + HO_2$	9.55E+06	2.00	3.970E+03
(19)	$H_2O_2 + OH = HO_2 + H_2O$	1.00E+12	0.00	0.000E+00
	$H_2O_2 + OH = HO_2 + H_2O$	5.80E+14	0.00	9.560E+03

Units are cm^3 mol s cal K. $k = AT^n\exp(-E_a/RT)$.

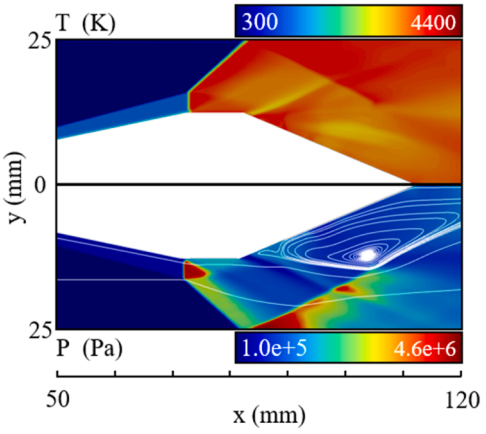

Fig. 2. Oblique detonation wave structures at $V_p/V_{CJ} = 1.5$.

when the projectile velocity decreases to slightly above the Chapman–Jouguet detonation velocity. Although the position of the triple wave point is almost unchanged, the angle of the oblique detonation wave is obviously increased. Correspondingly, the downstream wave gradually transitions from regular reflection [Fig. 3(b)] to Mach reflection [Fig. 3(a)]. In Fig. 3(a), the wave system from the projectile nose to the wall shows a transition from normal to oblique detonation and then normal detonation. In Fig. 3(b), the temperature and pressure distributions for both flow fields ($V_p/V_{CJ} = 1.2$ and 1.4) are similar, but no Mach stem appears when V_p/V_{CJ} is 1.4. The oblique detonation has a larger wave angle when the projectile velocity is V_p/V_{CJ} =1.2, which shifts the wave interaction position on the wall farther forward. Because the triple wave point of the Mach reflection is far from the wall, the area of the recirculation zone at the projectile tail is restricted by the more closed reflection shock. Correspondingly, the compression of burnt gas increases the average pressure at the bottom of the projectile. When V_p/V_{CJ} =1.4, the shock reflected by the wall is farther away from the projectile tail, which increases the recirculation zone area. Therefore, the compression effect on the burnt gas is reduced, which further leads to a thrust decrease for the projectile tail.

When the projectile velocity is decreased, the upper oblique detonation section gradually changes to a normal detonation surface. As shown in Fig. 4, the normal detonation can remain stable at 1.1 times the C–J detonation velocity instead of the actual C–J detonation velocity; therefore, the projectile is in the overdriven detonation mode [17]. The sound lines are marked to illustrate the flow features of this mode, and the region behind the detonation surface is also divided into two parts by the triple point. The region behind the upper detonation wave is the subsonic flow, which means the condition is overdriven and the wave surface is moving upstream. Meanwhile, the lower section is the supersonic flow preventing the movement of the upper section, and the wave system maintains a fragile stability. In this state, no reflected oblique shock is generated. Although the burned gas cannot be compressed by the reflected shock, the pressure of the burned gas is much

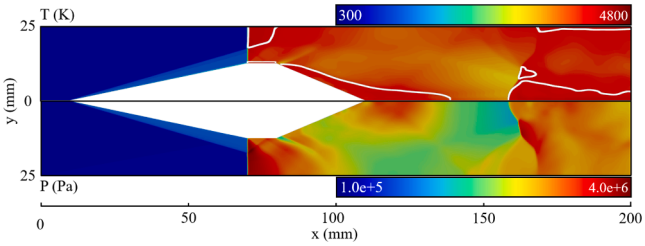

Fig. 4. Temperature distribution of the sub-detonative (thermally choked start) mode ($V_p/V_{CJ} = 1.1$).

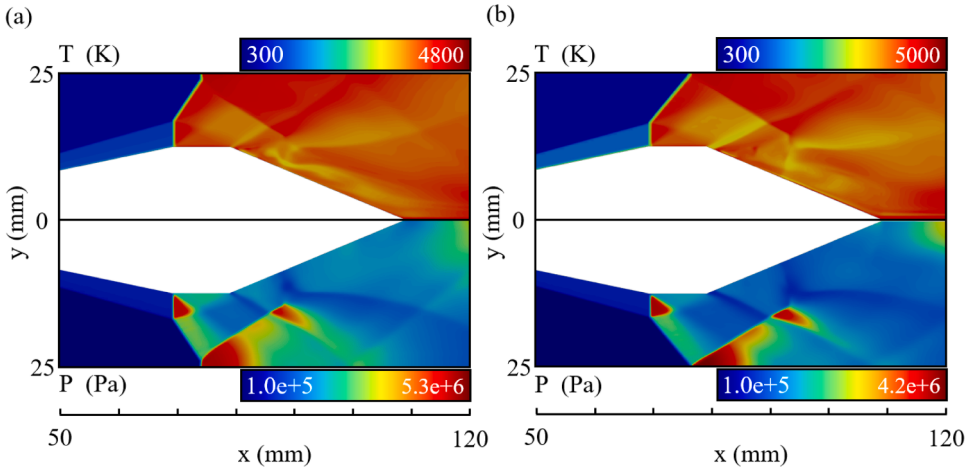

Fig. 3. Detonation wave structures at V_p/V_{CJ}=1.2 (a) and 1.4 (b).

higher than before owing to the overdriven normal detonation; therefore, the pressure near the projectile tail is higher than in the oblique detonation mode.

To quantify the condition differences between the projectile body and the tube wall, Fig. 5 shows the curves of the pressure, temperature, and horizontal velocity along the projectile body and at $y = 25$ mm. The post-shock temperatures of the two parts are comparable, but their pressures and velocities exhibit substantial differences. In the lower part [Fig.5(a)], the compression wave produces a less intense pressure than the detonation wave. The overall pressure is lower because there is also an expanding wave. The temperature and pressure oscillate downstream of the expanding wave. Moreover, the reverse velocity indicates that a recirculation zone is still generated close to the projectile body.

When the projectile velocity is decreased to the C–J detonation velocity, an unsteady structure appears, unlike the case $V_p/V_{CJ} = 1.1$. Fig. 6 shows the unstable detonation surfaces from 100 to 300 μs and the sound-line distribution for $t = 200$ μs. As seen from the wave dynamics, a typical oblique detonation is first induced at $t = 100$ μs. The detonation surface moves upstream throughout the process and becomes a normal detonation at $t = 200$ μs. Compared with the sound lines of Fig. 4, the two sections behind the detonation surface both form the subsonic flow, which means the entire detonation is in the overdriven state. Therefore, the surface movement does not stop until it exceeds the computational boundary or the detonation decays to the C–J state. For the upstream-moving detonation, the pressure before the conical ramp is significantly higher than that of the conical tail, which causes the projectile velocity to drop rapidly.

The flow field remains almost unchanged when the velocity is high enough to generate a regular reflection of oblique detonation. Fig. 7 shows similar results for V_p/V_{CJ} =1.8 and 2.0, where the main difference is the reflected shock position. The recirculation zone at $V_p/V_{CJ} = 2.0$ is much larger, and its pressure distribution is more even owing to the weakened confinement flow. As the shock wave position deviates, the flow field near the projectile tail is almost unaffected by it, so the thrust on the projectile tail is basically unchanged. Raising the projectile velocity to $V_p/V_{CJ} = 2.2$ induces a very strong shock wave, as shown in Fig. 8. The explosion occurs before the conical ramp owing to the high post-shock temperature and pressure, which leads to a sharp increase in reverse thrust.

To study the influence of changing speed on the ram accelerator thrust, a series of flow structures were simulated by adjusting the projectile velocity from $0.8V_{CJ}$ to $2.4V_{CJ}$ with an interval of $0.1V_{CJ}$ and calculating the thrust force from the pressure integral on the whole projectile. The running speed of the ram accelerator is the most important parameter, greatly affecting the wave structure and, thus, changing the thrust force. As shown in Fig. 9, a reverse thrust is generated for $V_p \leq V_{CJ}$, which results in the lower dilution-limit unstart.

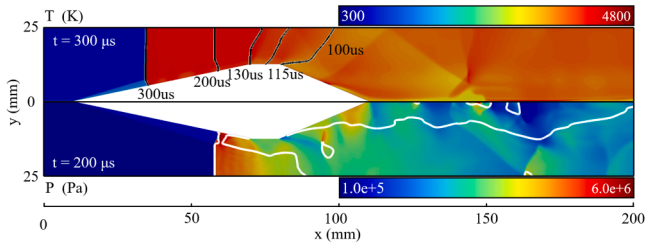

Fig. 6. Unstart evolution of detonation waves at V_p/V_{CJ}=1.0.

This unstart is caused by the thermal choking, and the overall reverse thrust can be calculated when the detonation surface has been driven ahead of the projectile. The reverse thrust reaches its maximum at $1.0V_{CJ}$. When the projectile velocity is lower than the C–J detonation velocity, the deceleration is gradual. The thrust force reaches its maximum at $V_p/V_{CJ} = 1.1$. The stabilized normal detonation is observed behind the nose (Fig. 4) with an overdriven-detonative mode. As the projectile velocity increases, the positive acceleration gradually decreases. The normal detonation first transforms into an oblique detonation wave, and then its surface gradually moves downstream (Fig. 3 and 7). At this stage, the projectile goes through trans-detonative mode [11] and super-detonative mode [13] operations. When V_P/V_{CJ} reaches 2.2, reverse acceleration occurs again owing to the enhanced compression of the oblique shock and induces a premature explosion. Similar results have been presented by Grismer et al. [18] whereby the dimensionless thrust (F_{net}) can be classified according to three specified heat-release values, and our results correspond to their cases with larger heat release. For large heat release, there are two distinct Mach numbers for which $F_{net} = 0$, and a perturbation at the lower Mach number results in a net force that accelerates the projectile away from the equilibrium Mach number.

For a projectile velocity in the range 1.1–2.1, decreasing the overall thrust cannot directly distinguish the trans-detonative and super-detonative modes. Clearly distinguishing those two modes requires analyzing the variation in the resistance on the projectile nose and the drag on the tail. The summary plots in Fig. 10 clearly show that the resistance on the nose increases almost linearly as the velocity increases, while the tail thrust drops rapidly and then flattens out. The weakening of the reflected shock's compression causes the average pressure to decrease, resulting in a decrease in tail thrust. When the reflected shock is far from the tail ($V_p/V_{CJ} \geq 1.5$), the flow in the recirculation zone is unaffected by its movement, and the pressure gradually stabilizes. Therefore, the decreasing tail thrust changes the acceleration of the trans-detonative mode, and the increase in resistance is the reason for the super-detonative mode.

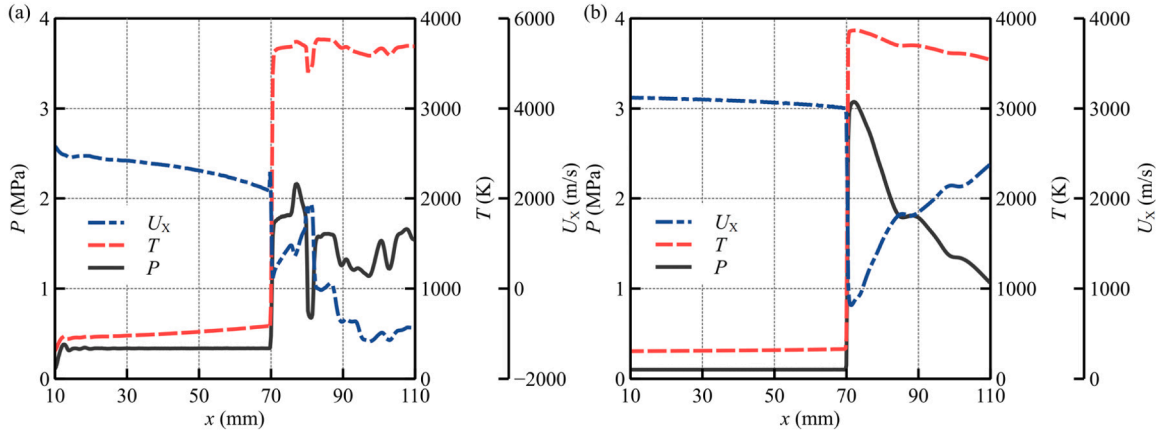

Fig. 5. Temperature and pressure distributions along the body and wall at V_p/V_{CJ}=1.1((a) along the projectile body; (b) at $y = 25$ mm).

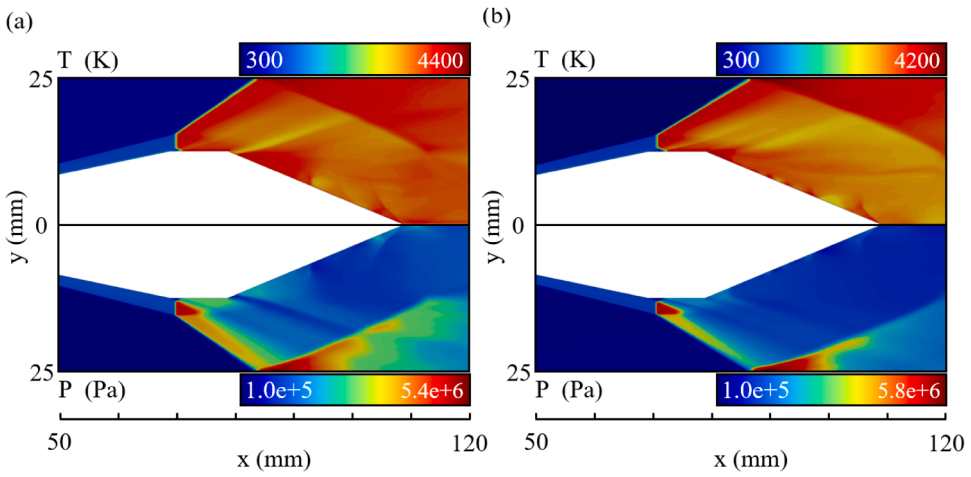

Fig. 7. Detonation wave structures at V_p/V_{CJ} = 1.8 (a) and V_p/V_{CJ} =2.0 (b).

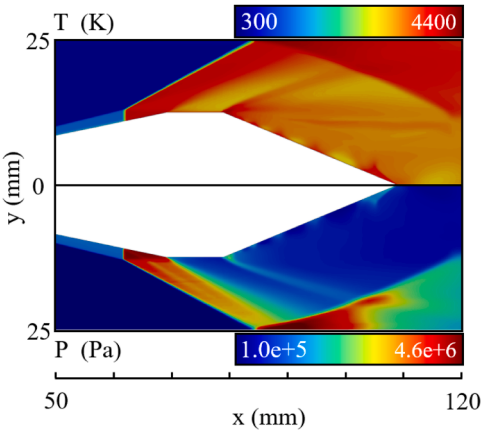

Fig. 8. Unstart super-detonative wave structures (V_p/V_{CJ}=2.2).

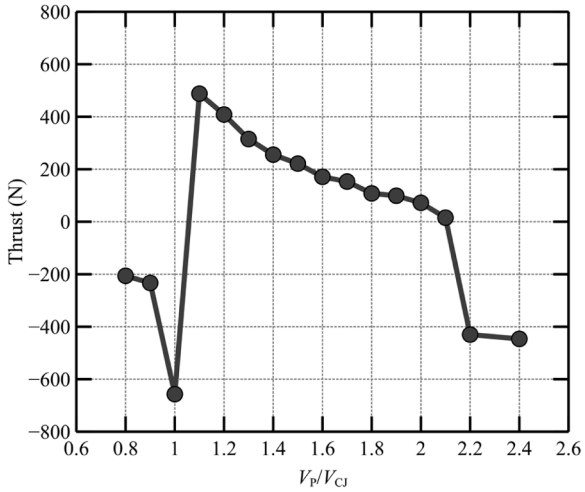

Fig. 9. Operation envelopes for a ram accelerator from the sub-detonative limit to the super-detonative limit.

Conclusion

The detonation structure, stability, and thrust of a ram accelerator flow were studied using compressible and reactive Navier–Stokes simulations. Simulating the wave system with a projectile velocity from 0.8 to 2.4 times the C–J detonation velocity indicated a stable operating range, yielding the following conclusions. For the oblique detonation mode, the triple point settles on the conical ramp with an abrupt transition, and the transverse wave is perpendicular to the ramp. The recirculation zone is restricted by the reflected ODW shock at the projectile tail, which generates a strong thrust force. When the initial velocity of the projectile increases, a series of detonation modes appears, including overdriven detonation, trans-detonation, and super-detonation. Overdriven detonation gives the maximum thrust at a lower starting velocity, and this thrust decreases as an ODW forms. The tail thrust of the super-detonation mode almost remains unchanged owing to the stability of the recirculation zone. At a higher velocity, the ignition before the conical ramp leads to an unstart.

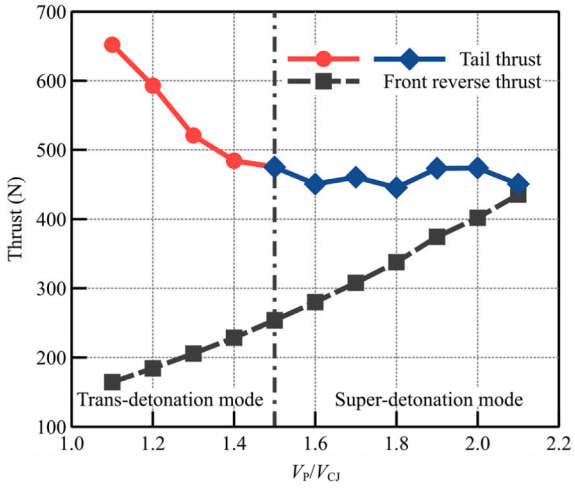

Fig. 10. Front reverse thrust and tail thrust for various velocities.

Declaration of Competing Interest

The authors declare that they have no known competing financial interests or personal relationships that could have appeared to influence the work reported in this paper.

Data availability

Data will be made available on request.

Acknowledgments

This research was supported by the National Natural Science Foundation of China (NSFC) (No. 12002041). Mark Kurban from Liwen Bianji (Edanz) (www.liwenbianji.cn) edited a draft of this paper.

Appendix

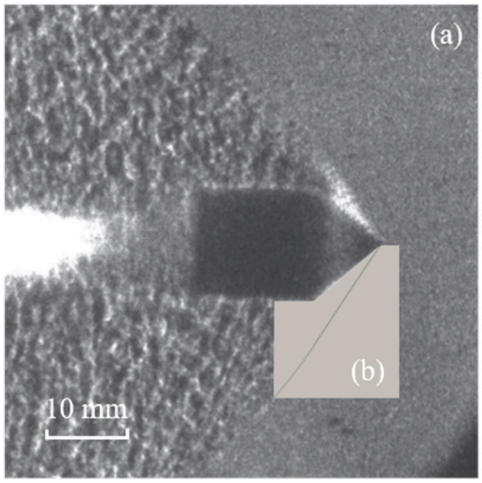

Fig. 11. Comparison of numerical and experimental flow fields: (a) Schlieren photograph of conical projectile detonation by Verreault [19], and (b) numerical temperature contour.

The reliability of the simulation was tested using Verreault's conical projectile detonation experiments [19]. Fig. 11 compares the temperature of the ODW structure from experimentally measurement and the simulation result. The leading shock exhibits similar structures in both the experiment and the simulation. The ODW angles obtained from the experiment and the simulation are 56° and 55.8°, respectively, which are in excellent agreement. (Fig. 13)

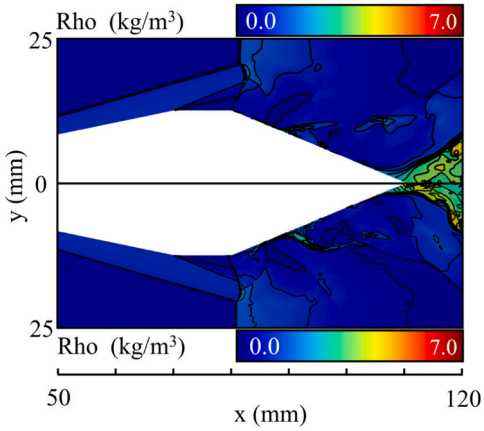

Fig. 12. Grid-independence studies with grid sizes of 100-μm (upper) and 50-μm (lower) at V_p/V_{CJ}=1.1.

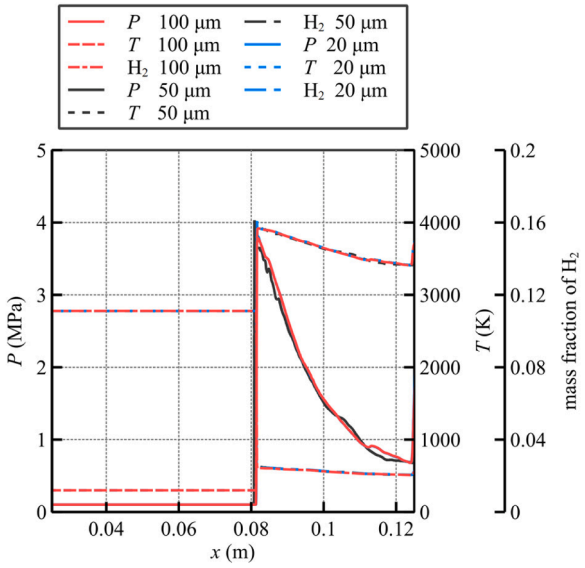

Fig. 13. Pressure, temperature, and mass fraction of H_2 along $y = 25$ mm with different grid sizes.

A study was performed to verify the simulation resolution. The flow fields in Fig. 11 are nearly the same with 100-μm and 50-μm grids, and it is difficult to see differences. The slight difference between the two results has no effect on the thrust or operational mode of the ram accelerator. A quantitative comparison is conducted by plotting the pressure and temperature along the line $y = 25$ mm in Fig. 12. This line corresponds to the flow on the normal detonation surface, which is most sensitive to the effect of grid size. No obvious differences are observed, and the curves nearly overlap with each other. Further simulations with grid sizes of 20 μm have been also conducted, illustrating almost the same flow fields. Studies [20,21] have shown that ODW simulations require less grid resolution than normal detonations, probably due to the unique flow characteristics of oblique detonations. Moreover, this study employs relatively overdrive factors for the main conditions, which significantly reduces the fine structures of detonation front. Therefore, in the following simulations a length scale of 100 μm was used, and important results were verified by refining the mesh. Therefore, a grid of 100-μm is sufficient to capture the main flow. Additionally, the residual error is plotted (on a log–log scale) against the mesh size in Fig. 14. The convergence falls close to the second order, demonstrating that the resolution used here is acceptable. The computational method employed effectively simulates oblique detonation wave shape and accurately calculates the thrust of the ram accelerator. Additionally, simulations of the cellular structure can be conducted using higher-order techniques [22,23].

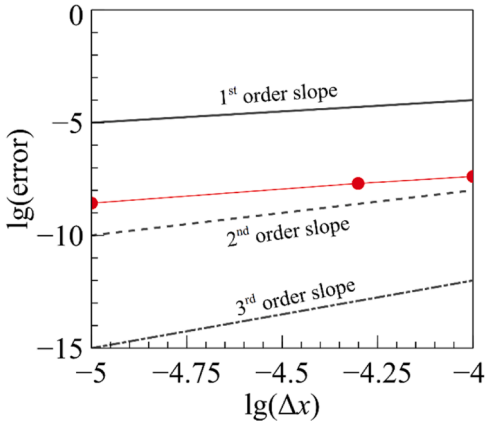

Fig. 14. Variation in residual error for different grid sizes.

References

[1] A. Hertzberg, A.P. Bruckner, D.W. Bogdanoff, Ram accelerator: a new chemical method for accelerating projectiles to ultrahigh velocities, AIAA J. 26 (1988) 195–203.

[2] D.W. Bogdanoff, Ram accelerator direct space launch system: new concepts, J. Propuls. Power 8 (1992) 481–490.

[3] F.K. Lu, H. Fan, D.R. Wilson, Detonation waves induced by a confined wedge, Aerosp. Sci. Technol. 10 (2006) 679–685.

[4] H. Teng, Z. Jiang, On the transition pattern of the oblique detonation structure, J. Fluid Mech. 713 (2012) 659–669.

[5] H. Teng, H.D. Ng, K. Li, C. Luo, Z. Jiang, Evolution of cellular structures on oblique detonation surfaces, Combust. Flame 162 (2015) 470–477.

[6] H. Teng, Z. Jiang, H.D. Ng, Numerical study on unstable surfaces of oblique detonations, J. Fluid Mech. 744 (2014) 111–128.

[7] K. Wang, P. Yang, H. Teng, Steadiness of wave complex induced by oblique detonation wave reflection before an expansion corner, Aerosp. Sci. Technol. 112 (2021), 106592.

[8] H. Teng, C. Tian, Y. Zhang, L. Zhou, H.D. Ng, Morphology of oblique detonation waves in a stoichiometric hydrogen-air mixture, J. Fluid Mech. 913 (2021) A1.

[9] H.F. Lehr, Experiments on shock-induced combustion, Astronaut. Acta 17 (1972) 589–597.

[10] A. Hertzberg, A.P. Bruckner, C. Knowlen, Experimental investigation of ram accelerator propulsion modes, Shock Waves 1 (1991) 17–25.

[11] A.J. Higgins, Ram accelerators: outstanding issues and new directions, J. Propuls. Power 22 (2006) 1170–1187.
[12] G. Xiang, X. Li, X. Sun, X. Chen, Investigations on oblique detonations induced by a finite wedge in high altitude, Aerosp. Sci. Technol. 95 (2019), 105451.
[13] J.Y. Choi, I.S. Jeung, Numerical simulation of super-detonative ram accelerator; its shock-induced combustion and oblique detonation, Hyperveloc. Launch. 10 (2016) 217–267.
[14] Q. Qin, X. Zhang, Controllable initiation characteristics of the oblique detonation wave in a combustor with a confined cone of a novel structure, Aerosp. Sci. Technol. 107 (2020), 106267.
[15] C.L. Bachman, G.B. Goodwin, Ignition criteria and the effect of boundary layers on wedge-stabilized oblique detonation waves, Combust. Flame 223 (2021) 271–283.
[16] M. Ó Conaire, H.J. Curran, J.M. Simmie, W.J. Pitz, C.K. Westbrook, A comprehensive modeling study of hydrogen oxidation, Int. J. Chem. Kinetic. 36 (2004) 603–622.
[17] C. Knowlen, A.P. Bruckner, D.W. Bogdanoff, A. Hertzberg, Performance capabilities of the ram accelerator, in: 23rd Joint Propulsion Conference, June 1987. AIAA Paper 87-2152.
[18] M.J. Grismer, J.M. Powers, Calculations for steady propagation of a generic ram accelerator configuration, J. Propuls. Power 11 (1995) 105–111.
[19] J. Verreault, A.J. Higgins, Initiation of detonation by conical projectiles, Proc. Combust. Inst. 33 (2011) 2311–2318.
[20] M.V. Papalexandris, A numerical study of wedge-induced detonations, Combust Flame 120 (2000) 526–538.
[21] H. Teng, Z. Jiang, H.D. Ng, Numerical study on unstable surfaces of oblique detonations, J. Fluid. Mech. 744 (2014) 111–128.
[22] X. Deng, B. Xie, R. Loubère, Y. Shimizu, F. Xiao, Limiter-free discontinuity-capturing scheme for compressible gas dynamics with reactive fronts, Comput. Fluid. 171 (2018) 1–14.
[23] X. Deng, B. Xie, H. Teng, F. Xiao, High resolution multi-moment finite volume method for supersonic combustion on unstructured grids, Appl. Math. Model. 66 (2019) 404–423.